

Monte Carlo Simulation of Three-Dimensional Nonisothermal Grain-Microstructure Evolution: Application to LENS Rapid Fabrication

R. S. Miller,¹ G. Cao,¹ and M. Grujicic²

A stochastic three-dimensional (3-D) model for grain-microstructure evolution during transient nonisothermal annealing of metallic materials is developed, validated, and applied to the LENS (Laser-Engineered Net Shaping) advanced rapid fabrication process. The model is based on the assumption that the main driving force for microstructure evolution is the reduction in energy contribution arising from the grain boundaries. A temperature-dependent grain-boundary mobility factor is introduced into the expression for the transition probability in order to account for nonisothermal effects, such as those induced by the rastering laser during LENS-based manufacturing. The grain-boundary mobility factor and its temperature dependence are determined using the available experimental isothermal-annealing data. The simulation of grain growth (under nonisothermal annealing conditions encountered in the LENS process) is carried out by coupling a Monte Carlo method for microstructure evolution with a finite difference-based solution to the three-dimensional (3-D) transient energy equation. In response to the computational challenges of the simulations, a highly efficient interprocessor communications methodology is developed, which greatly reduces the simulation time on parallel computers. The results obtained show that under isothermal annealing conditions, the kinetics of grain growth is governed by a temporal power-law behavior and that, after an initial transition period, the grain-size distribution (normalized with respect to the average grain size) becomes time invariant. Furthermore, the application of the model to the LENS process is found to enable establishment of the relationships between process parameters (the laser power, beam rastering velocity, etc.) and the microstructure (grain size distribution, depth of the heat-affected region, etc.) of the deposited material.

KEY WORDS: LENS rapid fabrication.

I. INTRODUCTION

Considerable experimental and theoretical efforts have been devoted to understanding the phenomenon of grain growth in metallic materials. The theoretical efforts can be broadly divided into three different approaches. The first approach is based on the solution of a continuum equation defined in the grain-size/time-space

subject to different assumptions regarding the mean growth velocity and its dependence on the grain size [1, 2]. The second theoretical approach to understanding the kinetics of grain growth is based on the use of the time invariance that a grain ensemble displays under isothermal annealing conditions. The time invariance is one of the defining characteristics of the normal grain growth and reflects the experimental observations that the grain-size distribution function is invariant in time when plotted as a function of the normalized grain size (the grain size divided by the arithmetic-mean grain size). After making additional assumptions regarding either the form of the grain-size distribution function [3] or the topology of the

¹ Department of Mechanical Engineering, Program in Materials Science and Engineering, Clemson University, Clemson, South Carolina 29634.

² To whom all correspondence should be addressed. email: mica@ces.clemson.edu

grain structure [4], the basic relations for the kinetics of grain growth are derived.

The third approach to the problem of grain growth involves the use of various computer simulation techniques [e.g., 5–8]. In some of these techniques, each grain is described by a single parameter, which represents the radius of a sphere with the equivalent volume as the grain in question, and the driving force for growth is assumed to be proportional to the pressure difference between grains [5, 6]. As an alternative approach to computer simulations of grain growth, stochastic methods such as the Monte Carlo method are employed [e.g. 7, 8]. These methods enable the simulation of grain growth in a microstructure obtained by metallographic examination of polished and etched metallic samples. In these simulations, the grain microstructure is mapped onto a discrete computational lattice to which random “grain orientations” are assigned. A statistical Monte Carlo procedure is then used to simulate the evolution of materials microstructure accompanied by grain growth. To date, such simulations have been limited to two-dimensional (2-D) and isothermal conditions.

Predictive capabilities in metallic grain growth have application in a wide diversity of fields. The present work is concerned with the LENS (Laser-Engineered Net Shaping) free-form fabrication process [9]. Free-form fabrication is one of the fastest growing manufacturing technologies, which has the potential of drastically reducing the time period between the initial conceptual design of a part and its actual fabrication [10, 11]. Among these technologies, the LENS fabrication process is unique in that it enables a direct fabrication of the parts made of metallic materials. A typical LENS system consists of a Nd:YAG laser, a controlled-atmosphere glovebox, a 3-D computer-controlled positioning system and several powder-feed units. The positioning system is located inside the argon-filled glovebox in which the oxygen level is generally held below 2–3 ppm. The laser beam enters the glovebox through a window mounted on the top of the glovebox and is directed to the deposition region using a focusing lens. Due to the high temperature of the laser beam, a small melt pool is created at the top surface of the depositing part into which the powder-feed system delivers the metallic powder.

In the LENS process, a part is built in a layer-by-layer fashion. To manufacture a part, 3-D solid model is first generated using a CAD (Computer-Aided Design) software package. The solid model is next sliced into thin layers and the file containing the information about the topology of each layer is used to drive the focusing lens and the powder-feed nozzle. As the focusing lens and the powder-feed nozzle raster the surface, a line of

the new layer is deposited. Typically, the width and the height of a deposition line are around 300 μm . After the fabrication of a new layer is completed, the positions of the focusing lens and the powder-delivery nozzle assembly are incremented in the positive vertical z direction by the height of a layer and the process is continued.

Cubes of the size comparable to the width/height of a deposition line ($\sim 300 \mu\text{m}$) can be considered as representative material elements, which contain the main microstructural features of the material deposited by the LENS process. Such representative material elements experience a very complicated thermal history during fabrication of the part. When one such element is first created, it contains a mixture of the metallic melt and solid (partially melted) powder particles. As the laser beam moves away, the element first solidifies, acquiring a fine (typically $\sim 2\text{--}3 \mu\text{m}$) nearly equiaxed grain structure and then continues to cool. The element is again subjected to high temperatures when the elements just above it in the next layer are deposited. This may cause partial melting of the upper portion of the element in question. However, the remainder of the element remains solid but exposed to very high temperatures approaching the solidus temperature of the metallic material. Under such conditions, significant coarsening of the material microstructure is quite probable, which can lead to a pronounced loss in material strength and ductility. As the laser beam moves away, the temperature of the element again decreases. The thermal cycling of a deposited material element described above continues, although with a progressively lower peak temperature, as additional layers are deposited.

The two primary objectives of the present work are: (1) to extend the 2-D isothermal Monte Carlo grain-growth model initially developed by Srolovitz and co-workers [7, 8], to 3-D and nonisothermal annealing conditions; and (2) to apply the model to the prediction of grain structure evolution in a representative material element of a metallic part produced by the LENS fabrication process. The Monte Carlo method is used since, as discussed above, it allows incorporation of the complexity of the grain-boundary topology, which is likely to play an important role under dynamic heating conditions produced by a rastering laser in the LENS process. The organization of the paper is as following: A detailed description of the Monte Carlo simulation model and of procedures used for the assessment of a grain-boundary mobility factor are presented in Section 2. The main results obtained are shown and discussed in Section 3. A list of main conclusions resulting from the present work is given in Section 4.

2. COMPUTATIONAL PROCEDURE

The 2-D Monte Carlo grain-growth simulation method, initially developed by Srolovitz and co-workers [7, 8], is extended in the third dimension and to non-isothermal annealed conditions and is utilized to analyze the evolution of grain microstructure during the LENS fabrication process. This statistical mechanics-based method has been previously used to analyze a number microstructural evolution processes, such as grain coarsening [7, 8], recrystallization [12, 13], etc. Following Tikare *et al.* [14], the original isothermal method of Srolovitz and co-workers [7, 8] is modified to enable the analysis of grain growth under complex laser-rastering induced thermal conditions in a material fabricated by the LENS process. As mentioned earlier, a 3-D analysis of grain growth is carried out in the present work. The results for an arbitrary planar cut through the representative material element can be readily compared with their experimental counterparts obtained using the quantitative metallographic examination of the corresponding (polished and etched) metallic sample.

As discussed earlier, a representative material element deposited during the LENS process has a characteristic linear dimension of around 300 μm . Hence, a $300 \times 300 \times 300 \mu\text{m}$ cube-shaped computational domain is selected for simulation. The domain is divided into $N = 300 \times 300 \times 300 = 27,000,000$ cubic cells, all of the same size. It is next assumed that there are $Q = 100$ different crystallographic orientations that each cell can have (sensitivity of the results to the value of Q is addressed in Section 3.1). Each cell is then assigned an initial crystallographic orientation by selecting a random integer q_i from the set 1–100 (inclusive). Since the mean grain size after solidification of the melt pool is around 2–3 μm and the grains are fairly equiaxed, the initial configuration of cells is annealed isothermally using the Monte Carlo method, until the mean grain radius reaches a value of $\sim 2.0 \mu\text{m}$. This configuration is assumed to be representative of the as-cast microstructure in a LENS-fabricated material. Last, the as-cast configuration is subjected to a typical thermal history associated with a rastering laser in the LENS fabrication process and evolution of the grain size and grain-size distribution are analyzed.

The Monte Carlo method used in the present work entails knowledge of the total energy of the computational domain, which is defined as:

$$E = \frac{1}{2} \sum_{i=1}^N \sum_{j=1}^n [1 - \delta(q_i, q_j)] \quad (1)$$

where n (set equal to 26 in the case of 3-D and to 8 in the case of 2-D simulations) is the number of nearest neighbors of a cell and δ is the Kronecker delta defined

as $\delta(q_i, q_j) = 1$ for $q_i = q_j$ and $\delta(q_i, q_j) = 0$ otherwise, with q_i and q_j denoting the orientation parameters of the neighboring cells i and j . It should be noted that the energy given by Eq. (1) contains only the grain-boundary contributions and that the grain-boundary energy is assumed to be independent of the misorientation of the adjacent grains and of the orientation of the grain boundaries. Hence, this equation can be strictly applied only to one-component, single-phase metallic systems with fixed, isotropic grain-boundary energies.

The Monte Carlo simulations of the grain growth process, both 3-D and 2-D, are carried out using the following steps:

- (1) The energy of the computational domain is computed using Eq. (1).
- (2) A cell is selected at random and a new possible crystallographic orientation of the cell is chosen at random from the set of crystallographic orientations of its 26 neighbors (8 neighbors in the case of 2-D simulations).
- (3) The total energy of the computational domain with the cell in question in its new crystallographic orientation is calculated using Eq. (1) and the difference between this energy and the one calculated in step (1), ΔE , is computed.
- (4) The energy change ΔE is next used to compute the transition probability for the cell in question as:

$$P = M_{gb}(T) \begin{cases} = 0 & \text{for } \Delta E > 0 \\ = 1 & \text{for } \Delta E \leq 0 \end{cases} \quad (2)$$

where M_{gb} is a temperature-dependent grain-boundary mobility factor and T is the temperature of the cell in question. The mobility factor M_{gb} in Eq. (2) is used to explicitly handle the effect of temperature on the grain-boundary velocity, V_{gb} . The two quantities, V_{gb} and M_{gb} , are generally considered to be proportional to each other [14]. It should be noted that a small departure from the original model of Srolovitz and co-workers [7, 8] is made in Eq. (2). That is, Srolovitz and co-workers [7, 8] used $P = \exp(-\Delta E/k_B T)$ (k_B is the Boltzmann's constant) expression for the transition probability when $\Delta E > 0$, instead of $P = 0$. However, the difference between the two models is expected to be insignificant, since for $k_B T \approx 0$ used by Srolovitz and co-workers [7, 8] $P = \exp(-\Delta E/k_B T)$ is of the order 10^{-18} or lower.

- (5) Once the transition probability P is computed, a random number R is generated in the range $0 - M_{gb}(T)$. The cell is allowed to change into the

new crystallographic orientation if $R \leq P$, otherwise the original cell orientation is kept.

- (6) The energy of the computational domain in the current configuration is assigned the step (1), and the procedure is continued starting with step (2).

In order to include nonisothermal material effects in a physically consistent manner, the above Monte Carlo procedure is coupled with the solution of the energy equation. It is well established that in microstructures with submicron characteristic dimensions, the classical Fourier heat transfer theory can break down [16]. In such cases, it may be necessary to account for the length-scale dependence of thermal conductivity along with the heat flux dependence on ballistic phonon-electron interactions. However, in the present calculations, the characteristic microstructure length scale is coarse enough that the temperature distribution within the material can be described by the macroscale Fourier conduction heat transfer equation as:

$$\frac{\partial T}{\partial t} = \frac{\lambda}{\rho c} \nabla^2 T \quad (3)$$

where λ is the thermal conductivity, ρ is the density, and c is the heat capacity and these properties are further assumed to be constants.

The energy equation, Eq. (3), is solved in conjunction with the grain-growth model discussed above using a second-order accurate explicit central-difference computational scheme. To ensure stability of the explicit scheme, the energy equation is solved with a time step Δt based on a diffusive Courant number of 0.15, which is calculated independently of the Monte Carlo simulation "time step." As will be discussed in Section 3.2, the Monte Carlo simulation time can be related to the corresponding physical annealing time using the experimentally determined grain-boundary mobility factor. In general, the ratio of the energy equation time step to the Monte Carlo time step is $\sim 10^5$.

Boundary conditions are applied to both the solution of the Monte Carlo procedure as well as to the energy equation in all three dimensions. The computational code developed allows the Monte Carlo simulations of grain growth to be carried out using either periodic or "interior cell" boundary conditions in any direction. The latter approach is needed to handle the free-surface boundary conditions where the number of the nearest neighbors of a cell is smaller than 26 (or 8 for 2-D simulations). For the energy equation, a choice of periodic, adiabatic, specified heat flux, or specified temperature distribution boundary conditions are available.

A parallel processing-based computation procedure is developed in order to address large domain resolutions with reasonable computation times. Toward that end, the computational domain is divided into a number (typically 8) of equally sized subdomains and the analysis of each subdomain is assigned to a separate CPU (central processing unit). The interprocessor communication required along the boundaries of adjoining subdomains is performed using MPI (message passing interface) libraries. Since, within the present 3-D model, the evolution of a cell is governed by its 26 nearest neighbors, a 1-cell layer is added to each face of all subdomains to provide the 26-cell environment for their boundary cells. The cells residing in the added layers are referred to as "ghost" cells. It should be noted that the ghost cells of one subdomain are also the boundary cells of the neighboring subdomains. In other words, the ghost cells of a subdomain are handled (updated) by CPUs other than the one handling the nonghost cells of the same subdomain. This implies that in order to ensure complete consistency between one and multiprocessor simulations, the neighboring processors must communicate with each other during each simulation step. In the most naïve approach, each processor would perform a single Monte Carlo event in parallel, followed by communication between all processors to update the ghost cells. This would normally make the computations prohibitively expensive as far more information is being communicated than is actually being operated on (i.e., for parallelization to be efficient, the extent of operations should substantially exceed the relative extent of communications).

In order to enhance the performance of the calculation, it is desirable to define some number of Monte Carlo operations, which will be conducted between updates of the ghost cells through interprocessor communication. To accomplish this, one must first understand the statistical nature of the potential errors, which may result by not updating the ghost cells after every event. A schematic displayed in Fig. 1 shows five adjacent subdomains, each handled by a separate CPU. Shading is used to denote the ghost cells associated with the subdomain, which is handled by the CPU 3. If a single cell is chosen at random from this subdomain, the only way that the ghost cells will affect the change in this cell (and, hence, interprocessor communication is required) is if the cell chosen is one of the border cells (e.g. cell A). The probability of this occurring is $P_1 = (2N_x + 2N_y) / (N_x \times N_y)$ where N_x and N_y are the numbers of cells in the x and y directions within the subdomain, respectively. If, indeed, one of the border cells is chosen, then its change will be affected by a neighbor subdomain only if that subdomain chooses as its next random cell one of the

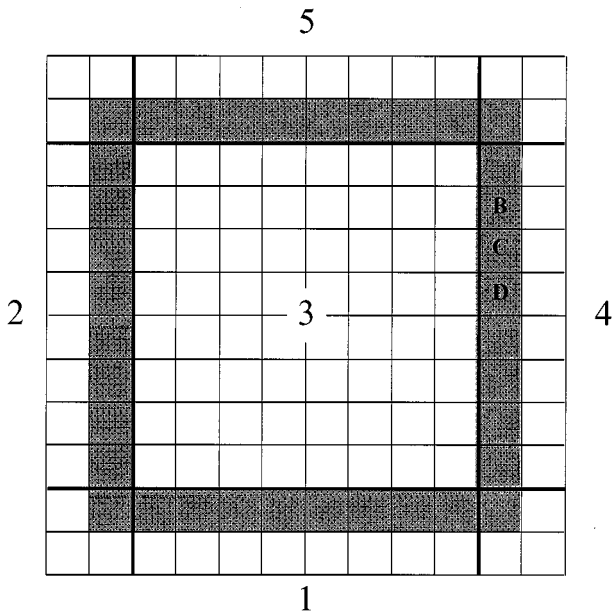


Fig. 1. A schematic of a computational subdomain (handled by CPU 3) and four adjacent subdomains (handled by CPUs 1, 2, 4, and 5). Shading is used to denote the ghost cells of the middle subdomain. One boundary cell (cell A) in the middle subdomain and its three (ghost) neighbor cells (B, C, D) are also denoted.

three neighbors (ghost cells B, C, D) to this cell. The probability for this event can be readily defined as $P_2 = 3/(N_x \times N_y)$. The approximate combined probability of both independent events occurring is, therefore, $P_3 = P_1 * P_2$, or, on average, one error (misfire) will result every $1/P_3$ Monte Carlo events if the ghost cells are not updated. It should be noted that this is a conservative estimate since it only predicts probabilities of choosing cells; however, errors will only occur if the cells are both chosen and their orientation values are changed. Finally, the number of Monte Carlo events that are allowed to occur between interprocessor communications is governed by an assigned probability of a single “misfire” occurring between communications, ER . For 2-D simulations, the procedure described above yields the following number of events allowed to occur between interprocessor communications:

$$N_{2D} = ER / (P_1 \times P_2) = ER(N_x \times N_y)^2 / [6(N_x \times N_y)]$$

For 3-D simulations, by direct extension, one obtains:

$$P_1 = \frac{[2(N_x \times N_y) + 2(N_x \times N_z) + 2(N_y \times N_z)]}{(N_x \times N_y \times N_z)}$$

$$P_2 = 9 / (N_x \times N_y \times N_z)$$

$$N_{3D} = \frac{ER / (P_1 \times P_2)(N_x \times N_y \times N_z)^2}{\{18[(N_x \times N_y) + (N_x \times N_z) + (N_y \times N_z)]\}}$$

As will be shown in the next section, the application of the above procedure reveals that a choice of $ER = 0.0001$ yields insignificant errors and allows for highly efficient calculations. The proper interpretation of this value is that, on average, only 1/10000 misfires result between ghost cell updates. As noted above, this is a conservative estimate since it assumes that all cells selected for the Monte Carlo operation will, in fact, change their orientations. In fact, this occurs only rarely once the grain structure develops, since the majority of cells within the domain will be within the interior of grains and have no chance of changing orientation.

3. RESULTS AND DISCUSSION

3.1. Isothermal Grain Growth

In this section, the 3-D Monte Carlo simulation method is first validated by carrying out a computer-simulation analysis of isothermal grain growth and comparing the results for the kinetics of the grain growth and for the grain-size distribution with their 2-D counterparts obtained by Srolovitz and co-workers [7, 8] and with theoretical predictions [1, 2]. In addition, since the Monte Carlo method will be used in the next section to analyze grain growth under dynamic, nonuniform temperature conditions encountered during the LENS fabrication process, the results of computer simulations of the isothermal grain growth process at several temperatures are compared with their experimental counterparts in order to determine temperature dependence of the grain-boundary mobility factor M_{gb} appearing in Eq. (2).

3.1.1. Temporal Evolution of the Mean Grain Size

Typical grain microstructures on a planar cut parallel to one of the faces of the computational domain obtained after isothermal annealing at the same temperature for two different times are shown in Figs. 2(a) and (b). The simulation time, t^* , in Figs. 2a and b is expressed in terms of the number of Monte Carlo Steps (MCS) where one MCS is defined as the number of computational steps equal to the total number of cells (27,000,000 in the present 3-D analysis) in the computational domain. It should be noted that in order to mimic the conditions encountered in an infinite crystal, all isothermal simulations of grain growth are carried out under periodic boundary conditions in all three directions.

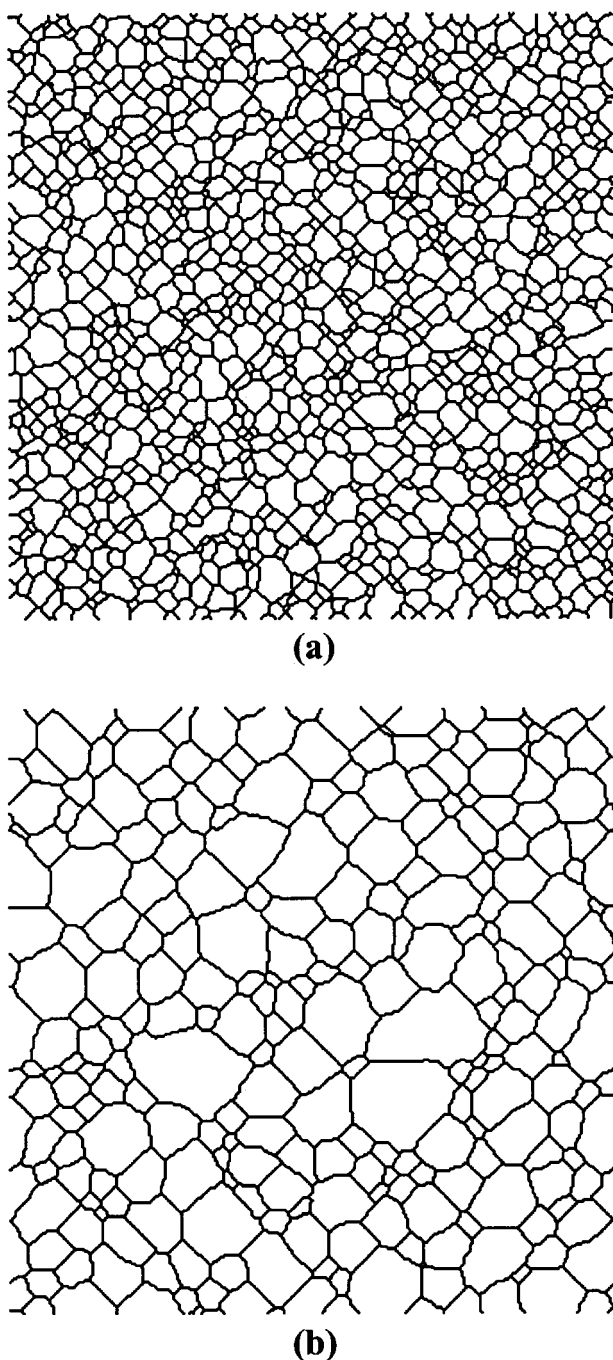


Fig. 2. Typical microstructures predicted by the 3-D Monte Carlo simulations of isothermal grain growth at the same temperature ($M_{gb} = 1.0$), but for two different simulation times: (a) $t^* = 100$ MCS; (b) $t^* = 500$ MCS.

The as-annealed grain microstructures shown in Figs. 2a and b contain grains of irregular, but fairly equiaxed shape. This observation is consistent with the approximation made in the present work that the grain boundary

energy is isotropic and constant throughout the computational domain. Qualitatively, the grain microstructure shown in Figs. 2a and b are analogous to the ones obtained by Srolovitz and co-workers [7, 8] who made a similar approximation regarding the nature of the grain boundary energy.

The kinetics of grain growth during isothermal annealing is generally found to be governed by the following time law:

$$\bar{R} = kt^n \quad \text{for} \quad \bar{R} \gg \bar{R}(t=0) \quad (4)$$

where \bar{R} is the arithmetic mean grain size (radius), t is the annealing time, and k is a constant, which exhibits Arrhenius temperature dependence. Despite significant scatter in experimental values for exponent n , a maximum value of 0.5 and a mean value around 0.45 are generally found for a variety of metallic materials [8]. To determine the mean grain radius, a search algorithm is developed which determines the number of adjacent cells of the same type which constitute each grain (i.e., the planar cut of each grain). Since the grains are fairly equiaxed, the radius of a grain is defined as the radius of a circle with an equivalent area as the cross-section area of the grain in question. The arithmetic-mean grain radius is then computed using a standard formula.

To determine if the predictions of the Monte Carlo method are consistent with the grain-growth kinetics law given by Eq. (4), the logarithm of the mean grain size \bar{R} is plotted against the logarithm of the simulation time in Fig. 3a. It should be noted that the simulation time, t^* , and the annealing time, t , are mutually proportional. The exponent n appearing in Eq. (4) can then be directly extracted from Fig. 3a as the slope of the $\log(\bar{R})$ vs. $\log(t^*)$ curve in the portion of the curve corresponding to $\bar{R} \gg \bar{R}(t=0)$ (dashed straight lines in Fig. 3a). The variation of the $d[\log(\bar{R})] / d[\log(t^*)]$ with $\log(t^*)$, averaged over 50 planar sections, is shown in Fig. 3b. To show the effect of potential misfires due to a lack of interprocessor communication during every Monte Carlo event, the results of three sets of 3-D simulations are shown in Figs. 3a and b. The three sets of results correspond, respectively, to the probability for misfire of $ERR = 0.0, 10^{-4}$, and 10^{-2} . It should be noted that in order to remove the effect of fine serrations, the $\log(\bar{R})$ vs. $\log(t^*)$ curves are first fitted to a fourth-order polynomial and the local slope of the $\log(\bar{R})$ vs. $\log(t^*)$ curve computed from the fitting polynomial. The results corresponding to the probability for the misfire of 0.0 and 10^{-4} are practically identical. Results corresponding to the probability of 10^{-2} differ slightly. Consequently, all subsequent 3-D simulations are done under the condition of the proba-

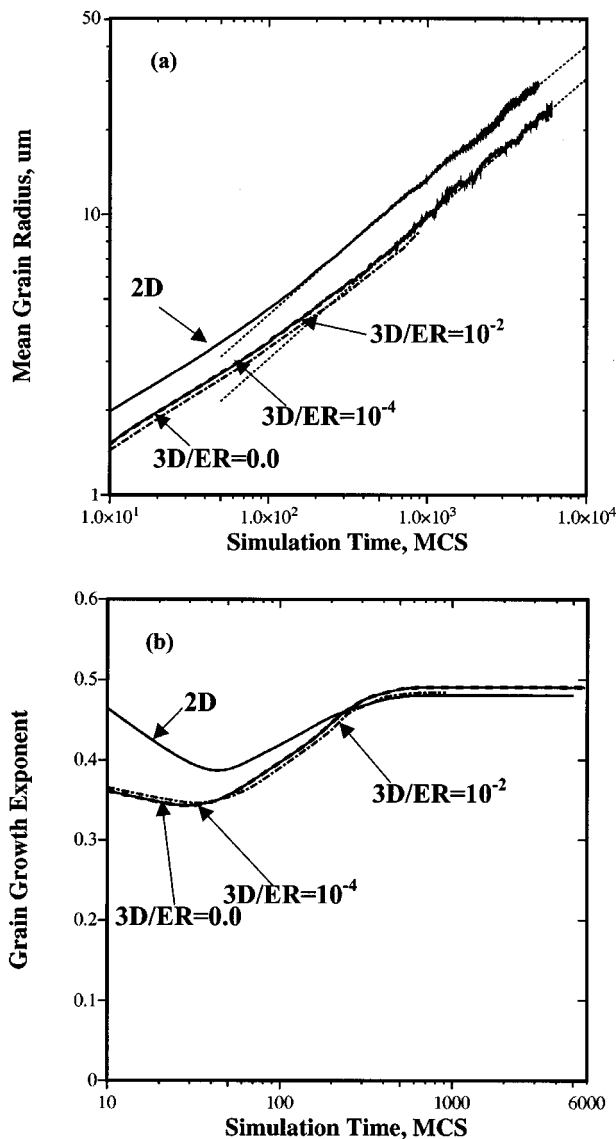


Fig. 3. (a) Evolution of the mean grain size with Monte Carlo simulation time; (b) evolution of the grain-growth exponent with Monte Carlo simulation time. Nomenclature: 2D, 2-D simulations; 3D, 3-D simulations; ER , number of acceptable misfires between interprocessor communications.

bility for misfire being 10^{-4} . This resulted in a substantial reduction of computation time without an apparent loss of computational accuracy.

Based on the results shown in Fig. 3b, the average value of the time exponent n (at longer simulation times) can be set to ~ 0.49 . This value is somewhat higher than the one (~ 0.43) reported by Srolovitz and co-workers [7, 8]. There are two potential explanations for the observed difference: (1) Srolovitz and co-workers [7, 8] car-

ried out 2-D simulations of grain growth; and (2) their simulations were carried out using triangular cells. To examine the role of the former, a 2-D analysis of grain growth using square-shaped cells is carried out in the present work. The results of this analysis are also displayed in Figs. 3a and b. The results displayed in Fig. 3b show that the present 2-D grain-growth simulation analysis yields a slightly lower value of the grain-growth exponent, $n = 0.48$. However, this value is still considerably higher than that reported by Srolovitz and co-workers [7, 8]. The difference can be, at least partly, attributed to the use of square-shaped cells in our work and the use of triangular cells by Srolovitz and co-workers [7, 8].

Srolovitz and co-workers [7, 8] reported that if the number of possible grain orientations, Q , is not large enough, it can affect the value of n . To determine the potential effect of the choice of Q on the grain-growth parameter, in addition to $Q = 100$, 3-D simulations are also carried out with $Q = 50$ and $Q = 200$. No systematic change in the magnitude of n with a change of Q is found and the average values for n obtained under the $Q = 50$, 100, and 200 conditions are essentially identical.

3.1.2. Evolution of the Grain-Size Distribution

It is well established experimentally that one of the defining features of grain growth is a pronounced homogeneity of the resulting materials microstructure. That is, the maximum grain size (expressed by the grain radius) is only 2.5–3 times larger than the arithmetic mean grain size, \bar{R} . In addition, when plotted as a function of the normalized grain radius R/\bar{R} , the grain-size distribution becomes time invariant.

To display the grain-size distribution function and its evolution during isothermal annealing as predicted by the 3-D Monte Carlo simulations, the probability density function is plotted in Fig. 4a vs. the logarithm of the normalized grain radius R/\bar{R} at five different simulation times. The results shown in Fig. 4a indicate that both the grain microstructure is quite homogeneous and that, with the exception of an initial transient period ($t^* < 300$ MCS), the distribution function is essentially independent of the simulation time. A comparison of the results shown in Fig. 4a with the ones shown in Figs. 3a and b indicates that the aforementioned steady-state distribution of grain size is attained approximately at the same time ($t^* \sim 600$ MCS) as that at which the power-law grain-growth exponent n attains its long-time value.

The grain-size distribution averaged over the last four simulation times indicated in Fig. 4a is shown as a histogram in Fig. 4b. The distribution peaks at $R/\bar{R} = 1.2$

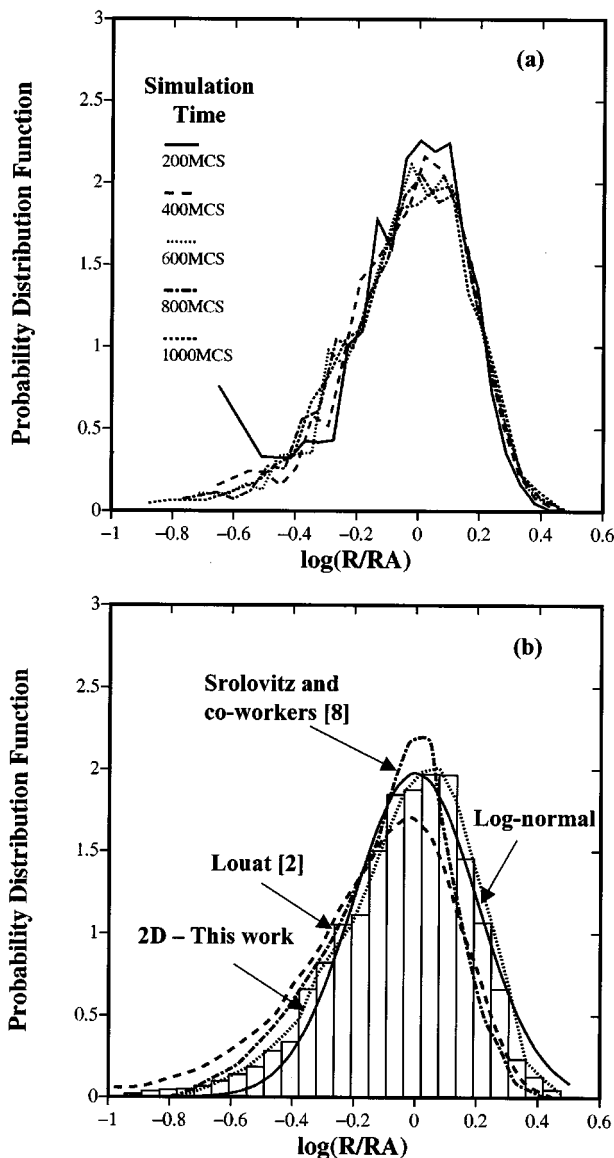


Fig. 4. (a) Evolution of the grain-size distribution function with Monte Carlo simulation time; (b) comparison of the present time-invariant grain-size distribution function (the histogram) with the log-normal, Louat [2] and Srolovitz and co-workers' [8] grain-size distribution functions.

$[\log(R/\bar{R}) = 0.08]$, has an apparent cut-off at $R/\bar{R} = 2.8$ [$\log(R/\bar{R}) = 0.45$], and asymptotically approaches zero as R/\bar{R} tends to zero. Also shown in Fig. 4b are two theoretical grain-size distribution functions.

The first theoretical distribution (shown as a solid curve) is the log-normal distribution [3] for which the probability distribution function is defined as: $(1/\sigma\sqrt{2\pi}) \exp[-(\log R/\bar{R})^2/2\sigma^2]$ (σ —the standard deviation). The log-normal grain-size distribution curve shown

in Fig. 4b is computed by employing the mean and standard deviation values of the present 3-D simulation-based distribution function shown in the same figure. While the two grain-size distribution functions agree reasonably well, there are noticeable differences: (1) The log-normal distribution function is symmetric in log-space and extends to $R/\bar{R} \rightarrow \pm\infty$. The Monte Carlo simulation-based distribution is, on the other hand, skewed and has an apparent upper cut-off value of R/\bar{R} ; (2) The simulation-based grain-size distribution peaks at $R/\bar{R} = 1.2$ rather than at $R/\bar{R} = 1.0$, as in the case of the log-normal distribution.

The second theoretical grain-size distribution function (shown as the dashed curve in Fig. 4b) is the function initially proposed by Louat [2]. The probability distribution function is, in this case, defined as: $R/\bar{R}[\exp-(R/\bar{R})^2/2]$ and, hence, does not contain any adjustable parameters. This function is in a somewhat better agreement than the log-normal distribution function with the one based on the Monte-Carlo simulations. In particular, the Louat grain-size distribution function has a tail in the limit $(R/\bar{R}) \rightarrow 0$ similar to the one predicted by the Monte Carlo simulations analysis. In addition, this function predicts an upper cut-off at around $R/\bar{R} \approx 2.7$ [$\log(R/\bar{R}) = 0.43$]. Nevertheless, the two distribution functions (the simulation-based and the Louat one) differ considerably with respect to both the magnitude and the location of the peak value of the probability distribution function.

Also shown in Fig. 4b (the dash-dot curve) is the grain-size distribution function obtained in the two-dimension simulation analysis carried out by Srolovitz and co-workers [7, 8]. The grain-size distribution predicted by Srolovitz and co-workers [7, 8] differs considerably from the one obtained in the present work using 3-D Monte Carlo simulations. Differences between the two distributions can be identified at: (1) small R/\bar{R} values, where the present results show a more pronounced tail, (2) near the peak of the probability distribution function, where the present results show a smaller magnitude of the peak and its position displaced toward larger R/\bar{R} values; and (3) in the upper R/\bar{R} cut-off region where the present results show a less sharp drop and a somewhat higher cut-off value of R/\bar{R} . The observed differences in the low R/\bar{R} distribution tail can be readily understood since, due to planar sectioning within the 3-D analysis, a grain of the considerable size can appear as a "small" grain on the plane of sectioning giving rise to a more pronounced low $-R/\bar{R}$ distribution tail. This conjecture is supported by the fact that the grain-size distribution function obtained in our 2-D simulation analysis (the dotted curve in Fig. 4b) also shows a shorter low $-R/\bar{R}$ distribution tail. The same phenomenon may be respon-

sible for the remaining difference between the 2- and 3-D grain-size distributions.

3.1.3. Assessment of the Grain-Boundary Mobility Factor

All isothermal annealing simulations discussed in the previous two sections are carried out under the condition $M_{gb} = 1.0$. This was justified by the fact that no effect of temperature on the kinetics of grain growth was analyzed. However, since the objective of the present work is to study the evolution of grain microstructure under complex thermal conditions encountered in the LENS fabrication process, it is necessary to assess the grain-boundary mobility factor and its temperature dependence. This assessment is carried out in the present work.

Figure 5a shows the experimental results (discrete symbols connected with a dotted line) of Feltham and Copley [15], pertaining to isothermal grain growth in Cu-10 wt. % Zn alpha brass. These results are used to demonstrate the procedure, which can be used to assess the grain-boundary mobility factor and its temperature dependence. The procedure involves the following steps:

1. The experimental results shown in Fig. 5a are replotted as $\log(\bar{R})$ vs. $\log(t)$ (the plot not shown for brevity), the resulting four curves (one curve for each annealing temperature) fitted to a linear relation, and the slope of the each line set equal to the grain growth exponent, n . This procedure yielded the average value of $n = 0.49 \pm 0.05$. To validate this value of n , the experimental results are replotted as $\bar{R}^{1/0.49}$ vs. t (discrete symbols) in Fig. 5b and analyzed using a linear regression analysis (the dashed straight lines).
2. Next, the experimental results are replotted as $\log[\bar{R}^{1/0.49}/t^0]$ vs. $1/T$, the results fitted to a linear function (the plot not shown for brevity) and the slope of the fitting line set to $-Q/R_g$, where Q is the activation energy and $R_g (= 8.314 \text{ J/(K*mole)})$ the universal gas constant. This procedure yielded $Q = 69.8 \text{ kJ/mole}$.
3. The maximum annealing temperature encountered during the LENS process is next set equal to the solidus temperature, T_{sol} , of the deposited material. For Cu-10 wt. % alpha brass $T_{sol} = 1250 \text{ K}$ is assumed. The grain boundary mobility factor M_{gb} is next set to 1.0 at T_{sol} . Since M_{gb} vs. T is assumed to be of an Arrhenius function in the form:

$$M_{gb} = A \exp\left(-\frac{Q}{R_g T}\right) \quad (5)$$

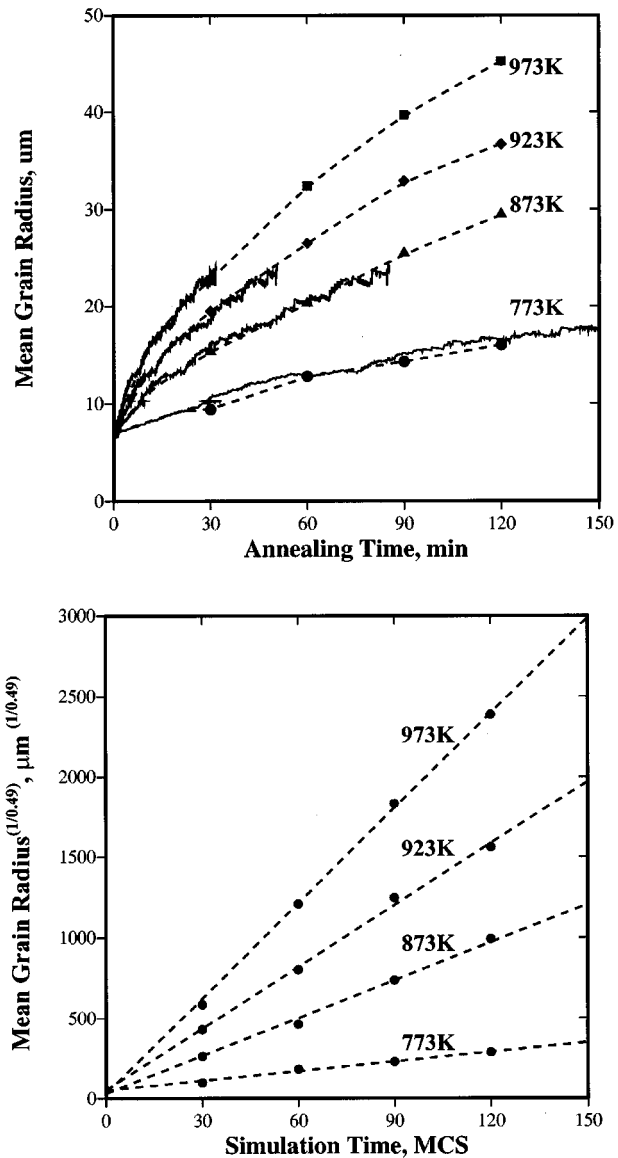


Fig. 5. Effect of annealing temperature and annealing time on the mean grain radius in Cu-10 wt.% Zn alpha brass [15].

the pre-exponential factor A can be derived from Eq. (5) and the condition $M_{gb}(1250 \text{ K}) = 1.0$. This procedure yielded $A = 826.4$ and the resulting temperature dependence of M_{gb} is shown in Fig. 6 (the curve denoted as “lower limit”).

It is frequently found [17] that the activation energy for chemical diffusion-based processes becomes higher at higher temperatures, making the temperature dependence of the respective kinetic parameters (the grain-boundary mobility factor in the present case) more pronounced. This finding is generally attributed to the fact that at

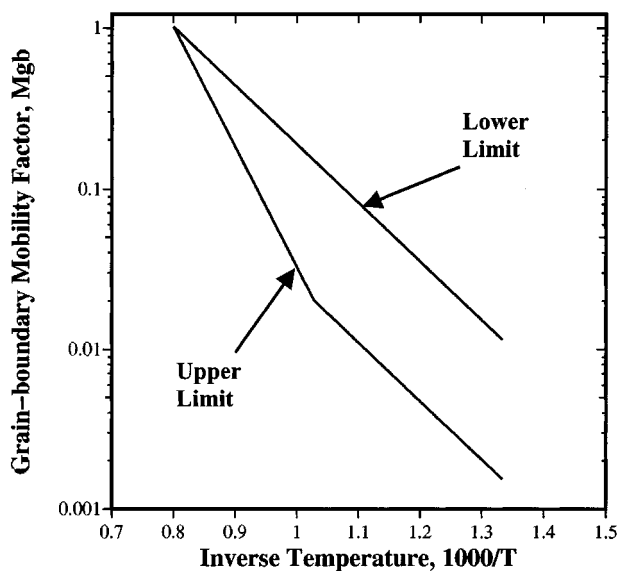


Fig. 6. Temperature dependence of the grain-boundaries mobility factor, M_{gb} , in Cu-10 wt.% Zn alpha brass.

high temperatures, the process kinetics is mainly controlled by bulk diffusion, while at lower temperatures, the process kinetics is dominated by grain-boundary diffusion. As a good approximation, the bulk-diffusion activation energy is generally taken to be twice the grain-boundary diffusion activation energy. In order to explore the effect of the higher activation energy at high temperatures, the previously determined activation energy (69.8 kJ/mole) is doubled, the transition between the low- and high-activation energy regimes assumed to take place at 973 K, and M_{gb} (1250 K) set to 1.0 again. The resulting M_{gb} vs. T relation is shown in Fig. 6 and is denoted as “upper limit.” The high-temperature portion of this relation is characterized with $A = 6.82 \times 10^5$ and $Q = 139.6$ kJ/mole, while the low-temperature portion of this relation is defined by $A = 111.7$ and $Q = 69.8$ kJ/mole.

3.1.4. Relationship Between Annealing and Simulation Times

In order to apply the grain-growth simulation model to the LENS process, one must establish the relationship between the physical annealing time (t) and the simulation time (t^*). The two times are related by a proportionality constant C , i.e., $t = Ct^*$. The constant C is determined so that the best agreement is obtained between the experimental results and the model predictions (Fig. 5a). It should be noted that the 3-D grain-growth analysis in Fig. 5a was carried out only until $\bar{R} \approx 25 \mu\text{m}$, since, at larger values of \bar{R} , the number of grains in the computa-

tional crystal became too small for a reliable grain-size statistics to be conducted. For the “lower-limit,” the grain-boundary mobility function C is found to be 1.1×10^{-1} sec/MCS, while for the “upper-limit,” the grain-boundary mobility function C is found to be 5.04×10^{-3} sec/MCS and 1.263×10^{-2} sec/MCS for 3- and 2-D analyses, respectively. The agreement between the \bar{R} vs. t functions predicted using either value of the proportionally constant C and the corresponding M_{gb} values and the experimental data is quite good, which validates the procedure used to determine both C and $M_{gb}(T)$.

3.2. Evolution of Grain Microstructure During LENS Processing

A schematic of the LENS fabrication process is shown in Fig. 7. The laser beam causes remelting of the very top layer of the depositing part (denoted as “remelted region” in Fig. 7), producing a melt pool into which metallic powder is injected. The combined effect of surface melting and powder injection yields fabrication of a new line (denoted as “new line” in Fig. 7). The region right beneath the remelted region (denoted as “region being studied” in Fig. 7) remains solid, yet exposed to high temperatures. It is the grain-microstructure evolution in this region that is analyzed in this section.

The laser beam used in the LENS process typically has a Gaussian distribution of the specific power with the center of the beam receiving the most power and the power progressively dropping off toward the beam edges. The cross section of the beam is generally circular or made slightly elliptical in order to increase the width of the depositing line. To simplify the calculation, only a

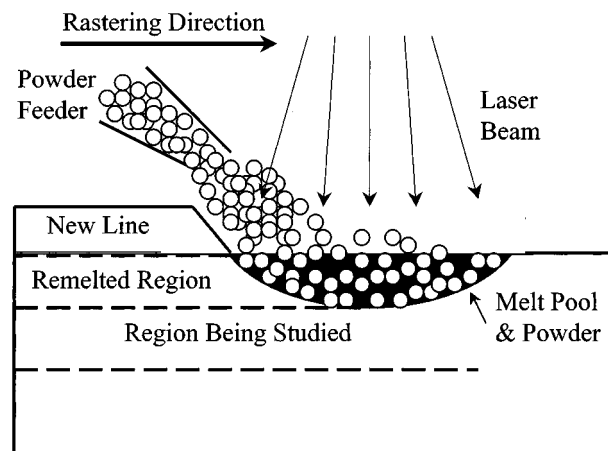


Fig. 7. A schematic of the LENS fabrication process.

laser beam with the circular cross section is considered in the present work. Two laser-beam diameters, 240 and 325 μm , are considered in the present work. In addition, the distribution of the specific laser power over beam cross section is assumed to be uniform. The (total) power of the laser used in the LENS fabrication process is typically in the range between 300 and 1000 W. A 750 W laser is used in all calculations carried out in the present work. The rastering velocity of the laser is generally in the range 500 $\mu\text{m}/\text{sec}$. At the lower-limit value of its rastering velocity (500 $\mu\text{m}/\text{sec}$) and for the characteristic length of the representative material element (300 μm), it takes the center of the laser beam 0.6 sec to traverse the element. Using the values for the annealing time/simulation time proportionally constant for Cu–10 wt.% Zn alpha brass determined in the previous section, the simulation time needed for the laser to traverse the characteristic material element is found to be 5.4 MCS (for the “lower-limit” form of the grain-boundary mobility function) and 119 MCS [for the “upper limit” form of $M_{gb}(T)$].

The computer simulation analysis of grain growth during the LENS fabrication process is carried out following essentially the same steps as those mentioned in the case of isothermal annealing except that, in addition to updating the crystallographic orientation of the cells, the 3-D energy equation, Eq. (3), is also solved in order to update their temperature. The main differences between the isothermal-annealing simulations discussed in Section 3.1.2 and the present (nonisothermal) annealing simulations pertain to the type of boundary conditions used. In the case of isothermal grain-growth simulations, periodic boundary conditions are applied in all three directions in order to mimic the grain-growth process in an infinite crystal. The evolution of grain microstructure during laser rastering, on the other hand, is carried out under boundary conditions corresponding to an isolated cubic region. Thus, cells located in the interior are considered to have 26 neighbors while those located on the faces, edges, and corners are assigned 17, 11, and 7 neighbors, respectively. The energy equation, Eq. (3), is solved under the following boundary conditions: (1) the circular region of the top face of the computational domain corresponding to the laser-beam cross section, is subjected to a fixed heat flux, while the remainder of the top face is subjected to a zero-flux condition; (2) for the remaining faces, the zero-flux conditions (i.e., $dT/dn = 0$, where n is a normal to the given face) are used. The use of the aforementioned adiabatic (zero-flux) boundary conditions appears appropriate considering the fact that, for the most part, the temperature of the nontop outer boundary of the computational domain remains close to the initial temperature. In addition, the temperature is not

allowed to exceed $T_{sol} = 1250$ K. In all cases, the initial temperature is taken to be uniform at $T = 500$ K. The following thermal and physical properties for Cu–10 wt.% alpha brass are used: $\lambda = 110$ J/(m/s/K), $\rho = 8800$ kg/m³, and $c = 372$ J/(kg/K).

The total path length of the laser is set equal to the sum of the representative material element length and the laser-beam diameter. At the beginning of each simulation run, the center of the beam is placed to the left of the representative material element, one laser-beam radius away from its left face. At the end of the run, the center of the laser beam resides outside the representative material element, one laser-beam radius away of its right face.

To obtain the as-cast microstructure, grain-growth simulations are initially carried out under isothermal conditions until the average grain diameter reached a value of approximately 4.0 μm . Figures 8a–c show the resulting grain microstructure on: (1) the top face of the representative material element; (2) the vertical plane, which is parallel to the direction of laser rastering and which bisects the representative material element (referred to in the following as the bisecting plane); and (3) the plane located halfway between the front face of the representative material element and the bisecting plane (referred to in the following as the second vertical plane). The results show a fairly equiaxed grain microstructure in all three planes which is, as discussed earlier, consistent with the isotropic grain-boundary energy approximation made in the present work.

When the “lower-limit” grain-boundary mobility factor is used, the simulation time (~ 5.4 MCS) was too short and, thus, no significant grain growth was found to result from laser rastering. Consequently, these results are not shown. In sharp contrast, when the “upper-limit” grain-boundary mobility factor is used, the simulation time extended to 119 MCS and visible grain coarsening was observed.

The temperature-distribution and grain-microstructure results corresponding to the time at which the laser beam has traversed one-third of its total path length are shown in Figs. 9 a–f. The direction of laser rastering is denoted in these figures by an arrow. The results shown in Figs. 9 a, c, and e pertain, respectively, to the temperature distributions on: (1) the top surface of the representative material element; (2) the bisecting plane; and (3) the second vertical plane. Figures 9b, d, and f show the corresponding grain microstructure results.

The temperature distribution on the top surface of the representative material element (Fig. 9a), shows a truncated circular region of a diameter of approximately 240 μm , within which the temperature attains its highest value (1250 K). Outside this region, the temperature

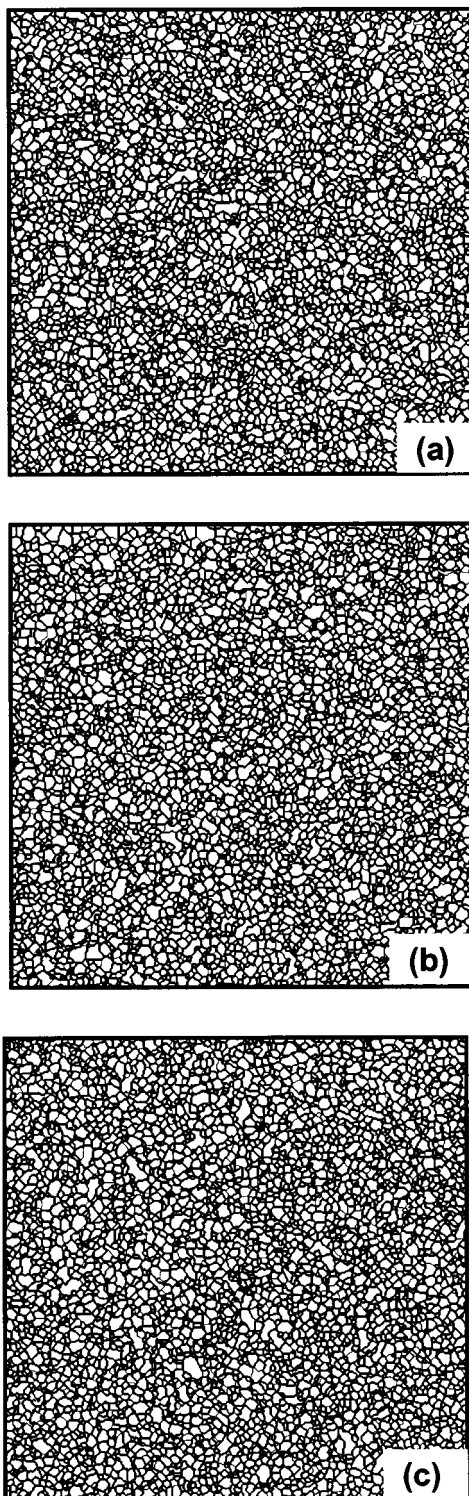


Fig. 8. The “as-cast” grain microstructure on: (a) the top face; (b) the bisecting vertical plane; and (c) the second vertical plane of the representative material element.

decreases quite rapidly. Consequently, at a distance of approximately $40\ \mu\text{m}$ ahead of the circular region, the temperature falls below $550\ \text{K}$. The temperature drop in the direction normal to the direction of laser rastering is equally rapid. The corresponding grain microstructure results. (Fig. 9b), show that significant grain growth takes place only in the truncated circular region associated with the highest ($1250\ \text{K}$) temperature. In addition, the most pronounced grain growth takes place in the horizontal, middle portion of this region. These findings are fully consistent with the previously discussed effects of annealing temperature and annealing time of the extent of grain growth. That is, the portions of the top surface of the representative material element outside the truncated circular regions are subject to the annealing temperatures, which are too low for the significant grain growth to take place. Furthermore, while the rim of the truncated circular region is exposed to the highest annealing temperature, the exposure time is relatively short, resulting in a significantly smaller extent of grain growth.

The temperature distribution on the vertical bisecting plane (Fig. 9c), shows that temperature decreases very rapidly in the depth direction. For instance, the temperatures higher than $1200\ \text{K}$ are localized in a $5\text{--}7\ \mu\text{m}$ thick topmost layer of the representative material element. The width of this region is approximately $140\text{--}160\ \mu\text{m}$. The corresponding grain microstructure result (Fig. 9d), show that again the significant grain growth takes place only in the portions of the representative material element exposed to the highest temperatures for a sufficient amount of time. Consequently, significant grain growth takes place only in a $\sim 10\ \mu\text{m}$ thick and $\sim 130\ \mu\text{m}$ wide upper left region of the representative material element.

The temperature distribution on the second vertical plane, (Fig. 9e), is qualitatively similar to the one shown in Fig. 9c. However, the depth ($4\text{--}6\ \mu\text{m}$) and the width ($120\text{--}140\ \mu\text{m}$) of the region with the temperature in excess of $1200\ \text{K}$ are somewhat smaller. The corresponding grain microstructure results, (Fig. 9f), show that again the significant grain growth takes place only in the $\sim 10\text{-}\mu\text{m}$ thick and $\sim 120\text{-}\mu\text{m}$ wide upper left portion of the representative material element, the portion which is exposed to the highest temperatures for a sufficient amount of time.

The temperature-distribution and grain microstructure results corresponding to the ones shown in Figs. 9a–f, but at the instant when the laser has completely traversed its total path length, are shown in Figs. 9a–f. A careful examination of the results displayed in Figs. 10a–f shows that the relationships between the magnitude of the annealing temperature, the duration of annealing, and

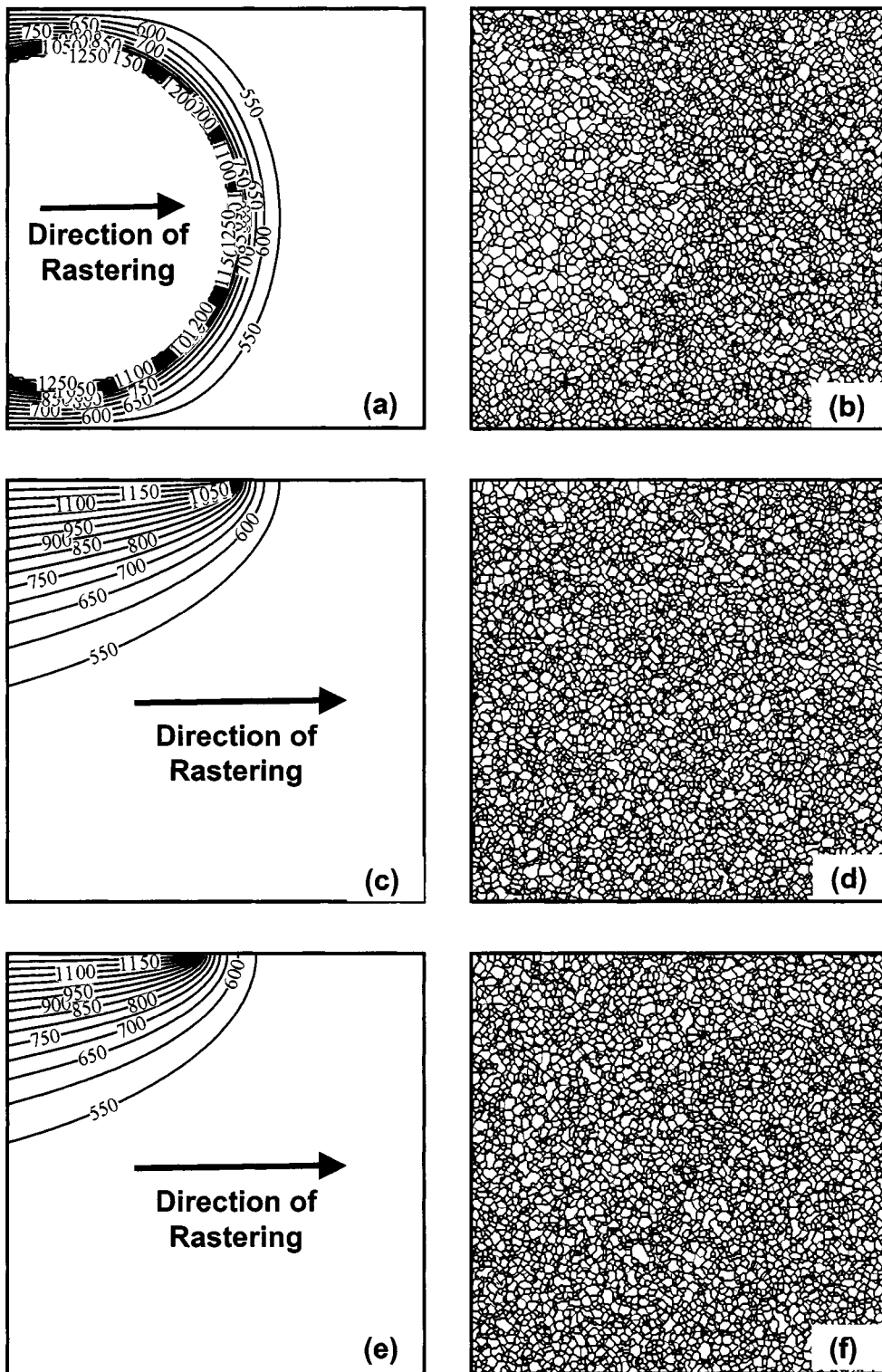


Fig. 9. Temperature distribution (a), (c), and (e) and the corresponding grain microstructure (b), (d), and (f) on: (a) the top face; (b) the bisecting vertical plane; and (c) the second vertical plane at the instant when the laser has traversed one-third of its total path length.

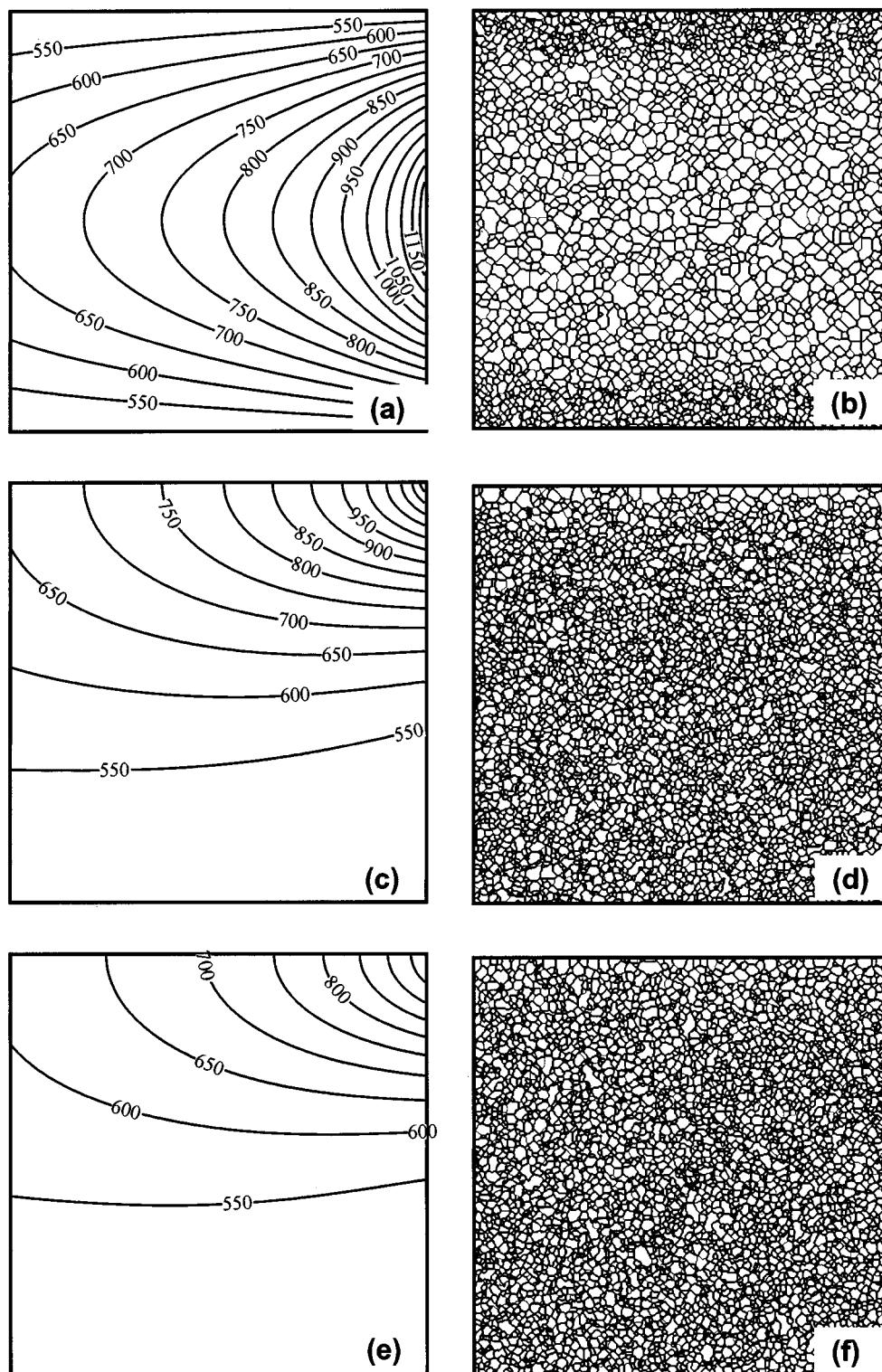


Fig. 10. Temperature distribution (a), (c), and (e) and the corresponding grain microstructure (b), (d), and (f) on: (a) the top face; (b) the bisecting vertical plane; and (c) the second vertical plane at the instant when the laser has traversed its entire path length.

the extent of grain growth, established in connection with the results shown in Figs. 9a–f are applicable also in this case. That is, significant grain growth takes place only in the topmost regions of the representative material element, which is subjected to the highest annealing temperatures and for the longest times.

The variation of the mean grain size (represented by the mean linear grain intercept) in the two vertical planes (Figs. 10d and f) with the distance from the top surface of the representative material element is shown in Fig. 11a. The two sets of results are, respectively, denoted as the “bisecting plane” and the “second vertical plane.” The

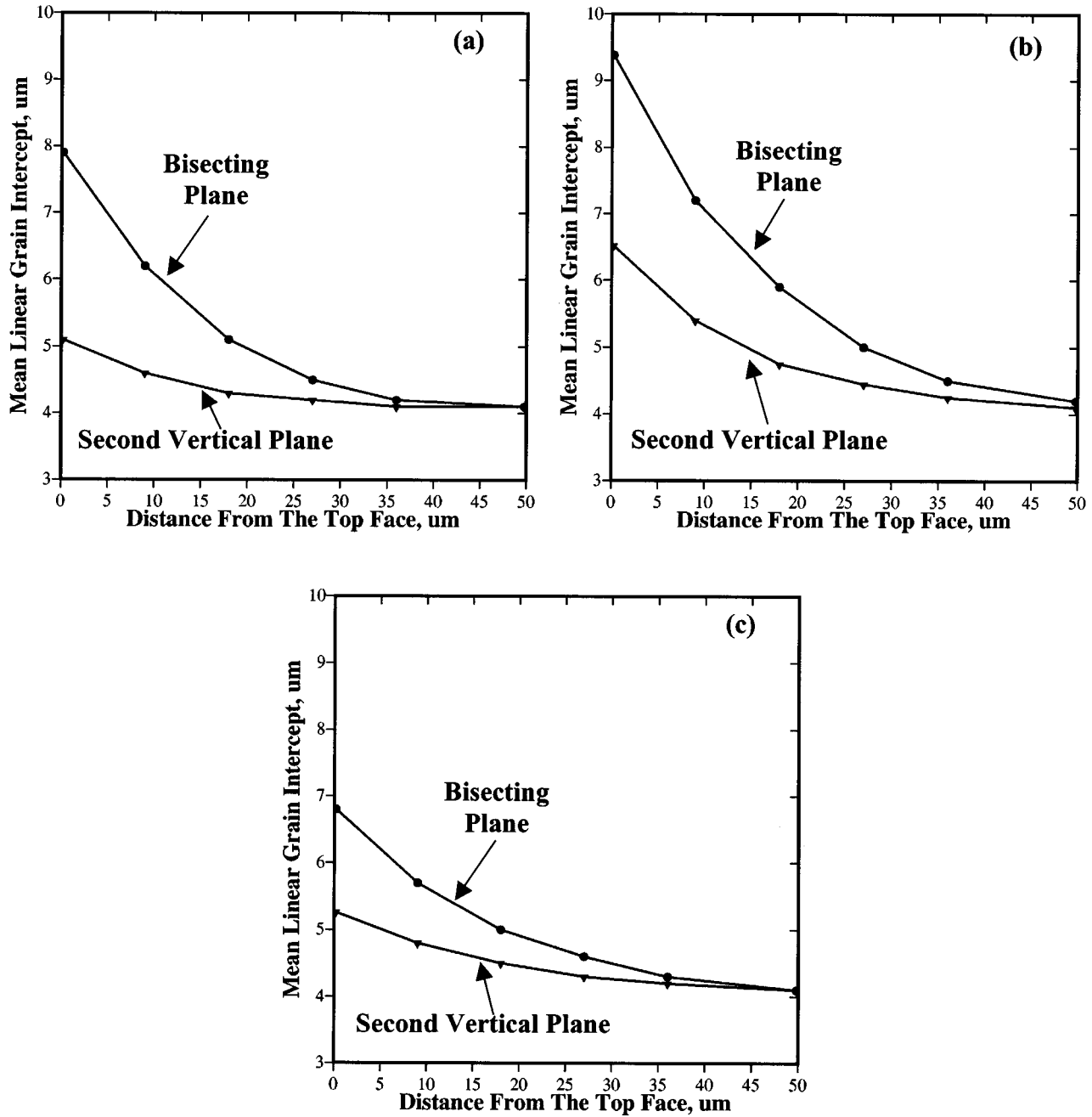


Fig. 11. Variation of the mean linear grain intercept with distance from the top face of the representative material element: (a) laser-beam diameter = 240 μm , rastering velocity = 500 $\mu\text{m}/\text{sec}$; (b) laser-beam diameter = 325 μm , rastering velocity = 500 $\mu\text{m}/\text{sec}$; and (c) laser-beam diameter = 240 μm , rastering velocity = 2000 $\mu\text{m}/\text{sec}$.

results shown in Fig. 11a indicate that the largest extent of grain growth takes place in the region where the top surface of the representative material element and the bisecting plane intersect. In the top portion of this region, the grain size has increased by a factor of near two. Furthermore, the results shown in Fig. 11a indicate that laser rastering affects grain microstructure only in the topmost 20–25- μm thick region of the representative material element.

To demonstrate the effect of the LENS process parameters on the grain microstructure, the variation of the mean grain size in the two vertical planes with the distance from the top surface of the representative material element for the laser-beam diameter of 325 μm (the laser-rastering velocity = 500 $\mu\text{m}/\text{sec}$) and for the laser-rastering velocity of 1000 $\mu\text{m}/\text{sec}$ (the laser-beam diameter = 240 μm) are shown in Figs. 11b and c, respectively.

A comparison of the results shown in Figs. 11a and b indicates that as the laser-beam diameter increases, not only the extent of grain coarsening on the top face of the representative material element increases but also the size of the region within which coarsening takes place. These findings are consistent with the fact that as the laser-beam diameter increases, the exposure time of a cell at the top face of the representative material element to the highest temperatures increase. In addition, the size of the region subjected to the highest temperatures also increases.

A comparison of the results shown in Figs. 11a and c indicates that as the laser-rastering velocity increases, the extent of grain coarsening on the top face of the representative material element decreases while the size of the region within which coarsening takes place does not change significantly. These findings are consistent with the fact that as the laser-rastering velocity increases, the exposure time of a cell at the top face of the representative material element to the highest temperatures decreases while the size of the region subjected to the highest temperatures remains essentially unchanged.

The results shown in Figs. 11a–c demonstrate how the model developed in the present work can be used to establish a direct link between the LENS process parameters and the resulting materials microstructure. Once such links are established, they can be used for optimization of the process itself, the fabricated material, or both.

4. CONCLUSIONS

Based on the results obtained in the present study the following main conclusions can be drawn:

1. The 3-D Monte Carlo method-based simulation analysis of grain growth under isothermal annealing conditions predicts a grain-size distribution function with a pronounced small grain-size tail, which is more consistent than either analytical or simulation 2-D analyses with the experimental observations.
2. Experimental results for the kinetics of grain growth under isothermal annealing conditions can be used to determine the grain-boundary mobility factor needed in the Monte Carlo method-based simulations of grain growth. However, since the grain-boundary mobility factor is highly temperature sensitive, its accurate determination entails experimental isothermal-annealing data for the entire temperature range of interest.
3. By combining the grain-growth simulation method with the solution procedure for the thermal energy equation, a computational tool can be developed, which enables the analysis of the effect of various parameters in a material manufacturing process (e.g., the LENS rapid fabrication process) on the resulting material microstructure.
4. When coupled with an optimization scheme, this tool can be further used to optimize the manufacturing process, the microstructure, and, thus, properties, of the material product, or both.

ACKNOWLEDGMENTS

The material presented here is based on work supported by the National Science Foundation, Grant Numbers DMR-9906268 and CMS-9531930 and by the U.S. Army Grant Number DAAH04-96-0197. The authors are indebted to Drs. Bruce A. MacDonald and Daniel C. Davis of NSF and Dr. David M. Stepp of ARO for the continuing interest in the present work. The authors also acknowledge the support of the Office of High Performance Computing Facilities at Clemson University.

REFERENCES

1. M. Hillert, *Acta Metall.* **13**, 227 (1965).
2. N. P. Louat, *Acta Metall.* **22**, 721 (1974).
3. P. Feltham, *Acta Metall.* **5**, 97 (1957).
4. F. R. Rhines and K. R. Craig, *Metall. Trans.* **5**, 413 (1974).
5. V. Yu. Novikov, *Acta Metall.* **26**, 1739 (1978).
6. O. Hunderi and N. Ryum, *Acta Metall.* **27**, 161 (1979).
7. M. P. Anderson, D. J. Srolovitz, G. S. Grest and P. S. Sahni, *Acta Metall.* **32**, 783 (1984).

8. D. J. Srolovitz, M. P. Anderson, P. S. Sahni, and G. S. Grest, *Acta Metall.* **32**, 793 (1984).
9. D. M. Keicher, J. E. Smugeresky, J. A. Romero, M. L. Griffith, and L. D. Harwell, *SPIE Conf. San Jose, California, Jan., 1997*, pp. 699.
10. M. Burns, *Automated Fabrication: Improving Productivity in Manufacturing* (Prentice Hall, Englewood, NJ, 1993).
11. T. Whohlers, *Proc. Rapid Prototyping Manufacturing '96 Conf.* (Society of Manufacturing Engineers, Dearborn, MI, 1996).
12. D. J. Srolovitz, G. S. Grest, and M. P. Anderson, *Acta Metall.* **34**, 1833 (1986).
13. D. J. Srolovitz, G. S. Grest, M. P. Anderson, and A. D. Rollett, *Acta Metall.* **36**, 2115 (1988).
14. V. Tikare, M. L. Griffith, E. Schlienger, and J. E. Smugeresky, *Proc. 1997 Solid Free-Form Fabrication Symposium, Austin, TX, 1997*, pp. 699.
15. P. Feltham and G. J. Copley, *Acta Metall.* **6**, 539 (1958).
16. M. I. Flik, B. I. Choi, and K. E. Goodson, *J. Heat Transfer* **114**, 666 (1992).
17. R. E. Reed-Hill and R. Abbaschian, "Physical Metallurgy Principles," 3rd ed (PWS-Kent Publishing Company, Boston, MA, 1992).